ACS SENSORS

pubs.acs.org/acssensors Article

Spatially Encoded Photonic Microsphere Lens Arrays with Deterministic Hotspaces Enabling Optofluidic Surface-Enhanced Raman Scattering Chip for Dynamic Monitoring of Multiple Biomarkers

Zhenyong Dong,‡ Xiaoxian Liu,‡ Tao Wu, Feixiang Zheng, Yukai Liu, Xiao Ren, Feng Xu, Lunbiao Cui, Yan-Qing Lu,* Rui Xiao,* and Guanghui Wang*

Cite This: https://doi.org/10.1021/acssensors.6c03453 Read Online

ACCESS | Metrics & More | Article Recommendations | Supporting Information

ABSTRACT: Real-time, quantitative dynamic monitoring of multiple biomarkers is urgently needed in clinical practice; however, conventional technologies are limited by cumbersome workflows and time-consuming operational procedures. Surface-enhanced Raman scattering (SERS) offers high sensitivity and molecular fingerprinting capability, but its application in dynamic monitoring is restricted by signal instability caused by signal irreproducibility arising from stochastic hotspot analyte spatial mismatches, and an exclusive reliance on endpoint measurements that precludes kinetic information extraction. Hence, we present an optofluidic SERS chip integrating spatially encoded photonic microsphere lens arrays (SE-PMLAs) with deterministic hotspaces to overcome these limitations. Through precise integration of gold nanoparticles onto microsphere lens surfaces, each functional unit achieves cascaded photonic−plasmonic coupling among photonic nanojets, whispering-gallery modes, and localized surface plasmon resonance, with near-field feedback reinforcement that transforms random hotspots into engineered, uniform hotspaces, delivering an average enhancement factor of 2.8×10^{10} and signal uniformity with a relative standard deviation below 5%. Using spatially encoded sensing, we demonstrate single-sample, synchronous high-throughput detection of influenza A/B viruses, adenovirus, and monkeypox virus, achieving limits of detection of 0.53 pg/mL, 128.85 copies/mL, 199.56 copies/mL, and 2.7 pg/mL, respectively. Crucially, the chip's ultrastable signal output enables a kinetic quantification model based on the initial binding rate, revealed a linear correlation between analyte concentration and its initial binding rate (i.e., slope). This approach achieves rapid, high-precision dynamic monitoring within 60 to 120s while expanding the linear detection range by two orders of magnitude. Ultimately, this chip delivers a robust, minute-level point-of-care solution for real-time pathogen screening and critical disease diagnostics.

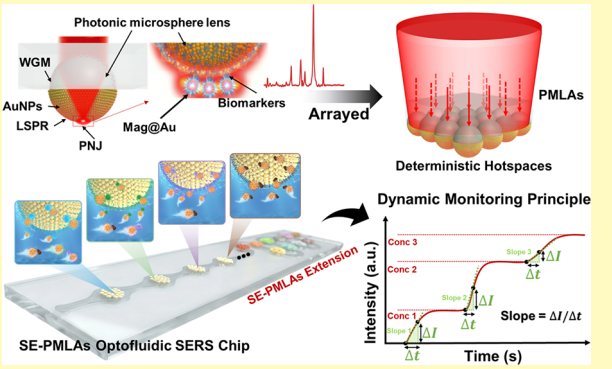

KEYWORDS: *surface enhanced Raman spectroscopy, optofluidic SERS chip, photonic microsphere-lens arrays, biomarkers, dynamic monitoring*

Real-time, quantitative biomarker detection is fundamental to early disease prediction and clinical diagnosis,[1−12] and key clinical scenarios such as early sepsis warning, real-time tumor treatment response assessment, and rapid screening of emerging infectious diseases urgently require continuous dynamic monitoring to guide therapeutic decisions. Existing techniques cannot fully meet this demand. Polymerase chain reaction (PCR) and enzyme-linked immunosorbent assay (ELISA) remain the gold standard but require laborious labeling and prolonged analysis and cannot perform multiplexed dynamic monitoring. Magnetic immuno-fluorescence assays deliver faster readouts but lack the spectral multiplexing capacity vital for complex biological matrices. Surface plasmon resonance (SPR) enables real-time kinetic analysis but offers limited sensitivity for low-concentration biomarkers.[13−19] In comparison, surface-enhanced Raman spectroscopy (SERS) has emerged as a transformative bioanalytical platform owing to its unique molecular fingerprinting capability, single-molecule sensitivity, and rapid spectral acquisition.[20−27] In particular, immuno-Raman strategies that functionalize plasmonic nanoprobes with specific Raman reporters exploit localized surface plasmon resonance (LSPR) to amplify signals dramatically, enabling ultrasensitive detection of trace biomarkers in complex samples.[28−36]

Although SERS offers distinct advantages in throughput, sensitivity, and multiplexing capacity, its application in dynamic monitoring remains constrained by fundamental technical

Received: July 24, 2026
Revised: October 4, 2026
Accepted: October 26, 2026

Downloaded from pubs.acs.org/ascef/article-pdf/doi/10.1021/acssensors.6c03453/6901836/se-2026-03453z.pdf by UNIV OF JINAN user on 29 October 2026

© XXXX American Chemical Society

bottlenecks. Most current SERS methods rely on endpoint measurements or semi-quantitative descriptions of dynamic trends, lacking standardized real-time dynamic analysis models and the ability to simultaneously capture dynamic changes across multiple spatial locations. An inherent spatial mismatch exists between the micron-scale excitation spot and the randomly distributed hotspots on SERS substrates; coupled with uneven sample deposition, this results in poor signal reproducibility. The signal collection process, which relies on external objective lenses, is constrained by their numerical aperture (NA), making it difficult to efficiently capture Raman-scattered photons at large angles and thus further limiting detection sensitivity. Importantly, in dynamic flow environments, these issues are markedly exacerbated, leading to significant signal drift and hampering precise quantitative kinetic analysis.

To achieve dynamic quantitative monitoring with both high sensitivity and long-term stability, microfluidic SERS chips integrated with dielectric microsphere lens arrays (MLAs) offer a promising route to the optical bottlenecks above. The microfluidic chip precisely controls the fluidic environment, while MLAs serve as efficient optical modulation elements.[37−40] MLAs partition a wide-field incident beam into thousands of sub-diffraction-limited photonic nanojets (PNJs), forming a dense array of ordered focal spots with ultrahigh optical power density.[41,42] These deterministic hotspaces replace the random hotspots and provide millimeter-scale coverage, directly resolving the reproducibility limit. The spherical geometry of the microspheres additionally supports whispering-gallery modes (WGMs) for enhanced field confinement and resonant Raman excitation,[43] and acts as a directional optical antenna that couples Raman-scattered photons from the nanoscale hotspot into the far-field collection path, resolving the NA-limited collection efficiency.[44,45] In a landmark study, Bao and coworkers demonstrated a cascaded photonic-plasmonic coupling strategy in which dielectric microspheres placed atop a plasmonic nanoarray generated electromagnetic hotspaces with a lateral extent exceeding 110 nm, enabling deep SERS profiling of intact small extracellular vesicles and validating that PNJs can efficiently drive LSPR.[46] However, their decoupled layer-by-layer assembly fabricates the microsphere layer and the plasmonic nanoarray independently before stacking, which renders the spatial alignment between the photonic and plasmonic components inherently probabilistic and precludes accurate quantitative analysis in dynamic flow.

In this work, we propose an optofluidic SERS chip integrating spatially encoded photonic microsphere lens arrays (SE-PMLAs) with deterministic hotspaces for the dynamic monitoring of multiplexed biomarkers. Through conformal nanofabrication, gold nanoparticles (AuNPs) are directly integrated onto microsphere surfaces, realizing deterministic three-mode optical synergy among PNJs, WGM and LSPR within each functional unit. Near-field feedback reinforcement transforms stochastic hotspots into uniform hotspaces, delivering an enhancement factor of 2.8×10^{10}. A spatially encoded PMLA sensor array was further constructed on a single chip. Upon a single injection, influenza A/B viruses, adenovirus, and monkeypox virus are synchronously captured by their corresponding encoded regions without cross-interference, achieving limits of detection of 0.53 pg/mL, 128.85 copies/mL, 199.56 copies/mL, and 2.7 pg/mL, respectively. A kinetic quantification model based on the initial binding rate method (IBRM) revealed a linear correlation between analyte concentration and initial binding rate (slope), enabling high-precision real-time tracking of minute-scale dynamic concentration changes of multiple biomarkers (RSD < 5%) and extending the linear dynamic range by two orders of magnitude. In summary, this work establishes a robust platform integrating stability, multiplexing capability, and real-time quantification, providing a transformative dynamic monitoring solution for the rapid diagnosis and precision treatment of infectious diseases.

RESULTS AND DISCUSSION

Sensing Mechanism of SE-PMLAs Optofluidics SERS Chip

The stable, multiplexed, and quantitative dynamic monitoring capability of the SE-PMLAs optofluidics chip arises from the synergistic combination of PMLAs optical regulation, spatial multiplexing for multiple detection, and the initial binding rate method for dynamic monitoring (Figure 1). The core of the chip lies in the PMLAs designed as fundamental sensing units. Through precise nanofabrication, AuNPs were conformally integrated onto the microsphere lens surfaces, forming photonic microsphere lenses that allow the high-intensity localized optical fields (from PNJs and WGMs) to efficiently drive LSPR. These PMLs achieve nanoscale co-localization and functional synchronization between localized optical excitation and electromagnetic enhancement, transforming the random plasmonic hotspots of traditional SERS substrates into deterministic, reproducible hotspaces within each microsphere domain. Furthermore, owing to the inherent directional antenna effects (DAEs), the PMLA arrays capture Raman-scattered photons from the nanoscale plasmonic regions and channel them into the far-field optical pathway, substantially improving collection efficiency while mitigating inter-unit optical crosstalk.

For multiplexed biosensing, the PMLs were assembled into an ordered array incorporating four spatially separated PMLAs sensing regions on a single chip. Each region was functionalized with capture antibodies that specifically recognize influenza A virus (Flu A), influenza B virus (Flu B), adenovirus (ADV), or monkeypox virus (MPXV), establishing a spatially encoded platform. To enhance the specificity and sensitivity of detection in complex samples, antibody-modified Au co-decorated Fe_3O_4 nanotags (Mag@Au) were employed to specifically capture and enrich the target viruses. As the sample containing mixed analytes flows through the chip, each target is captured by the antibodies immobilized in its corresponding region, enabling single-injection, simultaneous, and crosstalk-free detection of multiple analytes and thereby enhancing detection throughput and efficiency. To resolve the quantification challenges in real-time monitoring, we further developed a kinetic analysis framework based on the initial binding rate method (IBRM). This model exploits the linear dependence of the Raman intensity of surface-bound biomarkers on time at the early stage of biomolecular interactions, extracting the slope of signal intensity vs time (the initial binding rate) as the basis for quantification. By avoiding the baseline drift that commonly occurs in long-term monitoring, the method shortens the detection time to 1 to 2 min and substantially broadens the dynamic range for quantitative analysis.

Sensing Performance Analysis of Photonic Microsphere Lens

In its bare state, the microsphere lens generates PNJs as the dominant optical feature (Figure S1). The high-index microsphere intrinsically supports high-quality-factor whispering-gallery modes

Downloaded from pubs.acs.org/ascef/article-pdf/doi/10.1021/acssensors.6c03453/6901836/se-2026-03453z.pdf by UNIV OF JINAN user on 29 October 2026

https://doi.org/10.1021/acssensors.6c03453
ACS Sens. XXXX, XXX, XXX−XXX

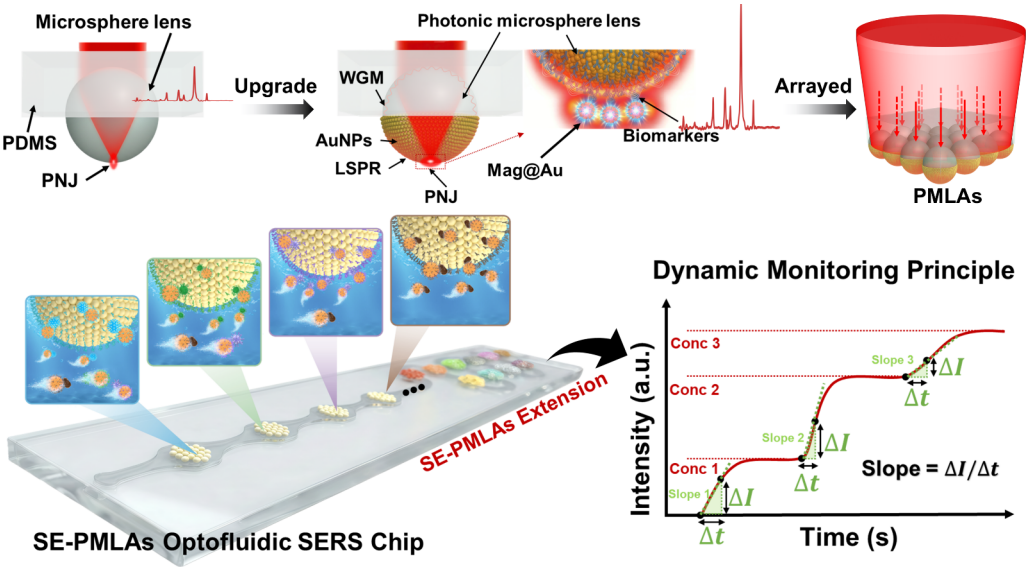

Figure 1. Sensing mechanism of SE-PMLAs optofluidics SERS chip. The chip is based on photonic microsphere Lens, which realize the high-intensity localized optical fields (from PNJs and WGMs) to efficiently drive localized surface plasmon resonances and enable highly efficient signal collection via the directional antenna effect of the PMLAs. These functionalized elements are assembled into a spatially encoded array for multiplexed target detection. By integrating the IBRM, the chip allows rapid, interference-free, and quantitative analysis.

(WGMs), but these modes remain dark under wide-field illumination because their excitation demands phase-matching conditions that the incident light cannot satisfy. Deposition of AuNPs overcomes this constraint, as the PNJs overlap with the surface-bound nanoparticles and excite LSPR in the interparticle gaps, and the oscillating LSPR dipoles, whose near-field resides within the microsphere evanescent field, couple into the WGM without phase-matching restrictions. The excited WGM field then feeds back to the AuNPs and further intensifies their LSPR oscillation. To verify this pathway, eigenfrequency analysis resolves a WGM resonance at 785 nm with a free spectral range of ≈4 nm. Scattering spectra further show a smooth Mie background with no WGM character for the bare microsphere, whereas the Au-decorated microsphere displays a circulating WGM field with sharp peaks at the WGM eigenfrequencies spaced by the free spectral range (Figure S2), directly demonstrating that the PNJ-excited LSPR excites the WGM. This cascaded PNJ-LSPR-WGM coupling establishes a dual enhancement cavity that drives strong SERS excitation of the surface-bound Mag@Au tags.

To quantify the enhancement on the actual detection system (Mag@Au tags conjugated to the PML surface), COMSOL simulations evaluated the average enhancement factor (AEF) of the Mag@Au construct within the PML localized fields. Comparison of the electric-field distributions under the PNJ-dominated, WGM-dominated, and synergistic modes shows that the PNJ-WGM synergy produces the most pronounced and uniform enhancement at the gold surface and adjacent nanogaps (Figure 2a and Figure S3). Integrating this enhancement over the microsphere surface yields an AEF of 2.8×10^{10}, three to four orders of magnitude higher than single-mechanism excitation. Moreover, the intrinsic antenna effect of the microsphere collimates the wide-angle Raman scattering from nanoscale hotspots into a narrow cone (±11.5°), enabling efficient far-field collection (Figure 2b,c). This dual capability of resonant excitation and directional emission underpins the ultrahigh sensitivity and signal-to-noise ratio of the photonic microsphere platform. Parametric simulations were further conducted to optimize the design. The PNJ focal point shifts outward as the microsphere diameter increases, and at ≈20 μm it coincides precisely with the outer microsphere surface, maximizing the driving efficiency of the AuNP LSPR (Figure 2d and Figure S4). The AuNPs size likewise governs the sensing performance, and the simulated AEF decreases with increasing particle size (Figure 2e and Figure S5). Because larger particles increasingly perturb the microsphere boundary and degrade the WGM quality factor, while also acting as a lossy barrier that attenuates Raman-scattered photons before directional collection (Figure 2f and Figure S6). Particles smaller than 10 nm, however, sustain insufficient LSPR field localization. We therefore selected 10 nm AuNPs, the smallest size that still maintains adequate LSPR enhancement and thus yields the highest AEF.

Based on the optimized design parameters, PMLs were assembled into PMLAs and their SERS performance was systematically evaluated. Spatially resolved mapping through point-by-point scanning at a 50 μm step generated a two-dimensional intensity map from the characteristic peak intensities, revealing high signal uniformity with a relative standard deviation (RSD) as low as 4.69% (Figure 2g). This confirms that precise control of geometric parameters and excitation conditions translates the theoretical high performance into large-scale uniform hotspot arrays, resolving the signal-fluctuation challenge of conventional SERS substrates. To assess manufacturing robustness, ten batches of PMLAs were independently fabricated by identical protocols, and detection of standard analytes at identical concentrations yielded an inter-batch RSD of 4.19% (Figure 2h). This batch-to-batch reproducibility demonstrates the high controllability and stability of the manufacturing process and ensures reliable data output in practical applications. Finally, malachite green (MG) was employed as a model Raman-active molecule for a systematic quantitative evaluation of PMLAs (Figure 2i–k). Across the three configurations, the LOD for MG improved

Downloaded from pubs.acs.org/ascef/article-pdf/doi/10.1021/acssensors.6c03453/6901836/se-2026-03453z.pdf by UNIV OF JINAN user on 29 October 2026

https://doi.org/10.1021/acssensors.6c03453
ACS Sens. XXXX, XXX, XXX–XXX

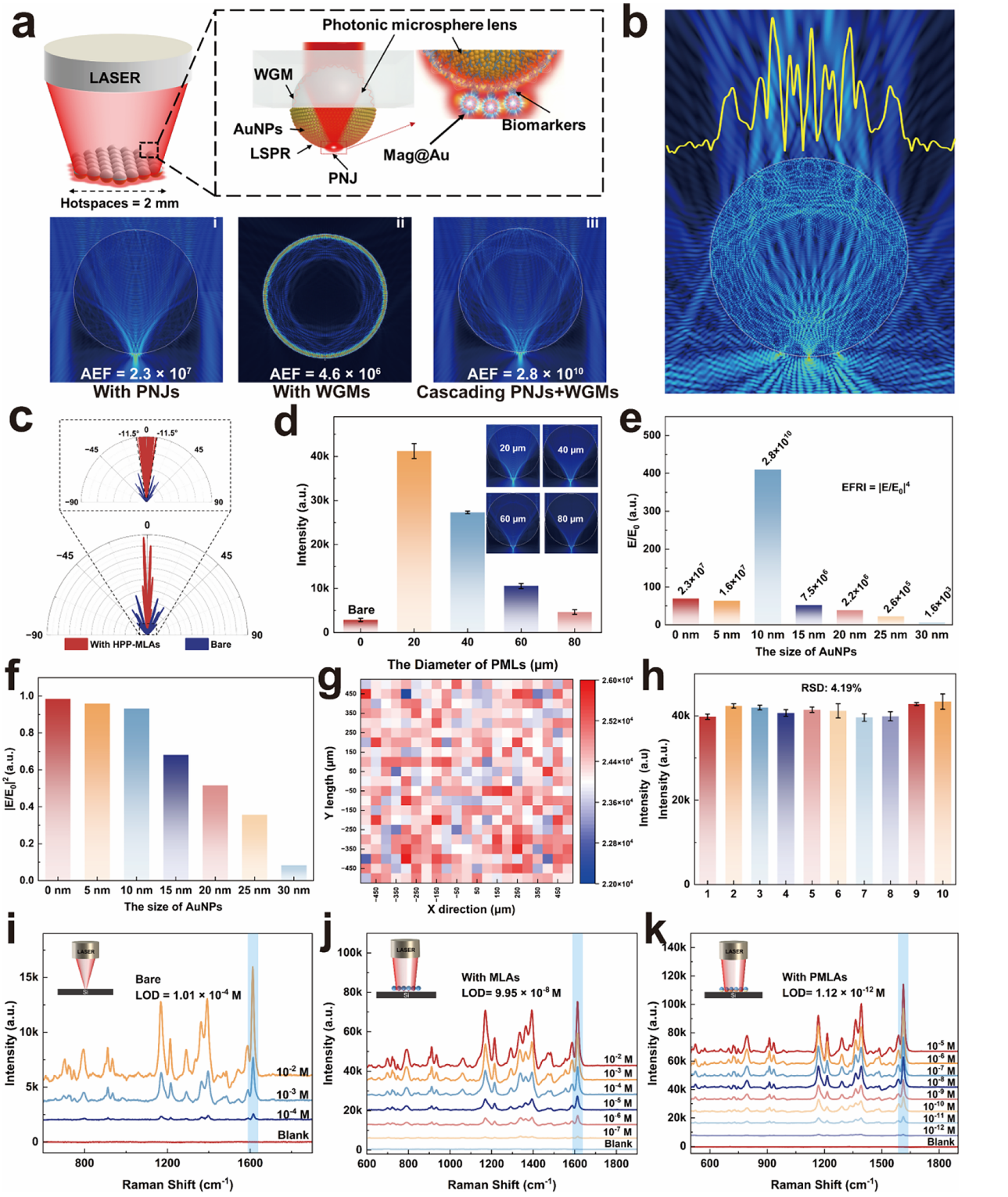

Figure 2. Synergistic enhancement mechanism, parameter optimization, and sensing performance of photonic microsphere Lens. (a) COMSOL Multiphysics simulations of electric field distributions revealing the optical synergy mechanisms in PMLs and the corresponding field distribution of Mag@Au positioned within the localized enhancement zone: (i) PNJ-dominated enhancement mode, (ii) WGM-dominated enhancement mode, (iii) synergistic coupling mode integrating both PNJ and WGM mechanisms. (b, c) Directional antenna effect characteristic of PMLs. (d) Effect of microsphere lens diameter on the focal position of the PNJs and its associated detection performance. Dual-aspect influence of AuNPs size on sensing performance metrics: (e) Effect on the average enhancement factor of Mag@Au, (f) Effect on the Raman signal collection power of PMLs. (g) Spatial Distribution Map of SERS Signals from a PMLAs. (h) Batch-to-batch reproducibility assessment of PMALs, confirming the high controllability and stability of the manufacturing process. Quantitative benchmark evaluation of detection performance across three distinct substrate configurations using malachite green as a model Raman-active molecule: (i) unenhanced silicon substrate, (j) bare MLAs without AuNPs surface modification, (k) gully functionalized PMLAs.

Downloaded from pubs.acs.org/ascef/article-pdf/doi/10.1021/acssensors.6c03453/6901836/se-2026-03453z.pdf by UNIV OF JINAN user on 29 October 2026

https://doi.org/10.1021/acssensors.6c03453
ACS Sens. XXXX, XXX, XXX−XXX

from 1.01×10^{-4} M on a bare silicon wafer, to 9.95×10^{-8} M on MLAs alone (whose PNJ focusing enhances detection without AuNP modification), and further to 1.12×10^{-12} M on PMLAs. This orders-of-magnitude improvement is attributable to the synergistic optical enhancement and the efficient collection enabled by the directional antenna effect.

Fabrication and Characterization of SE-PMLAs Optofluidics SERS Chip

SE-PMLAs were fabricated through a three-step process. First, four MLAs with an embedded depth of 10 μm were fabricated within the PDMS layer by vacuum-assisted self-assembly template hot-pressing. Unlike lithographic micro/nano-fabrication, whose rough surfaces degrade the WGM quality factor, self-assembly of pre-synthesized $BaTiO_3$ microspheres preserves smooth high-index spherical surfaces for high-Q WGMs and photonic nanojets. Second, a single layer of uniformly distributed AuNPs was deposited onto the MLA surfaces by vacuum plasma sputtering. Finally, the PMLAs were activated with 1-ethyl-3-(3-dimethylaminopropyl)carbodiimide (EDC)/N-hydroxysuccinimide (NHS) coupling chemistry to introduce carboxyl groups, followed by modification with different capture antibodies. Scanning electron microscopy (SEM) characterization confirmed that the MLAs were embedded to a depth of 10 μm (Figure 3b-i and Figure S7), the surface AuNPs exhibited a uniform particle size of 10 nm (Figure 3b-ii and Figure S8), and the virus-capturing Mag@Au particles were uniformly distributed across the PMLA surface, indicating successful antibody modification (Figure 3b-iii and Figure S9). These characterizations validate the feasibility and structural reliability of the PMLA-PDMS fabrication method.

Using standard soft lithography, we integrated SE-PMLAs (PDMS layer) with fluidic transport microchannels to fabricate an SE-PMLAs optofluidic chip for multiplex viral detection. In addition, channel height critically governs the adsorption of magnetic nanotags onto the photonic microspheres. A lower height shortens the diffusion distance of the nanotags toward the sensing interface and enhances convective transport, increasing the capture density, while the higher fluid shear stress in the confined space flushes away nonspecifically bound nanotags

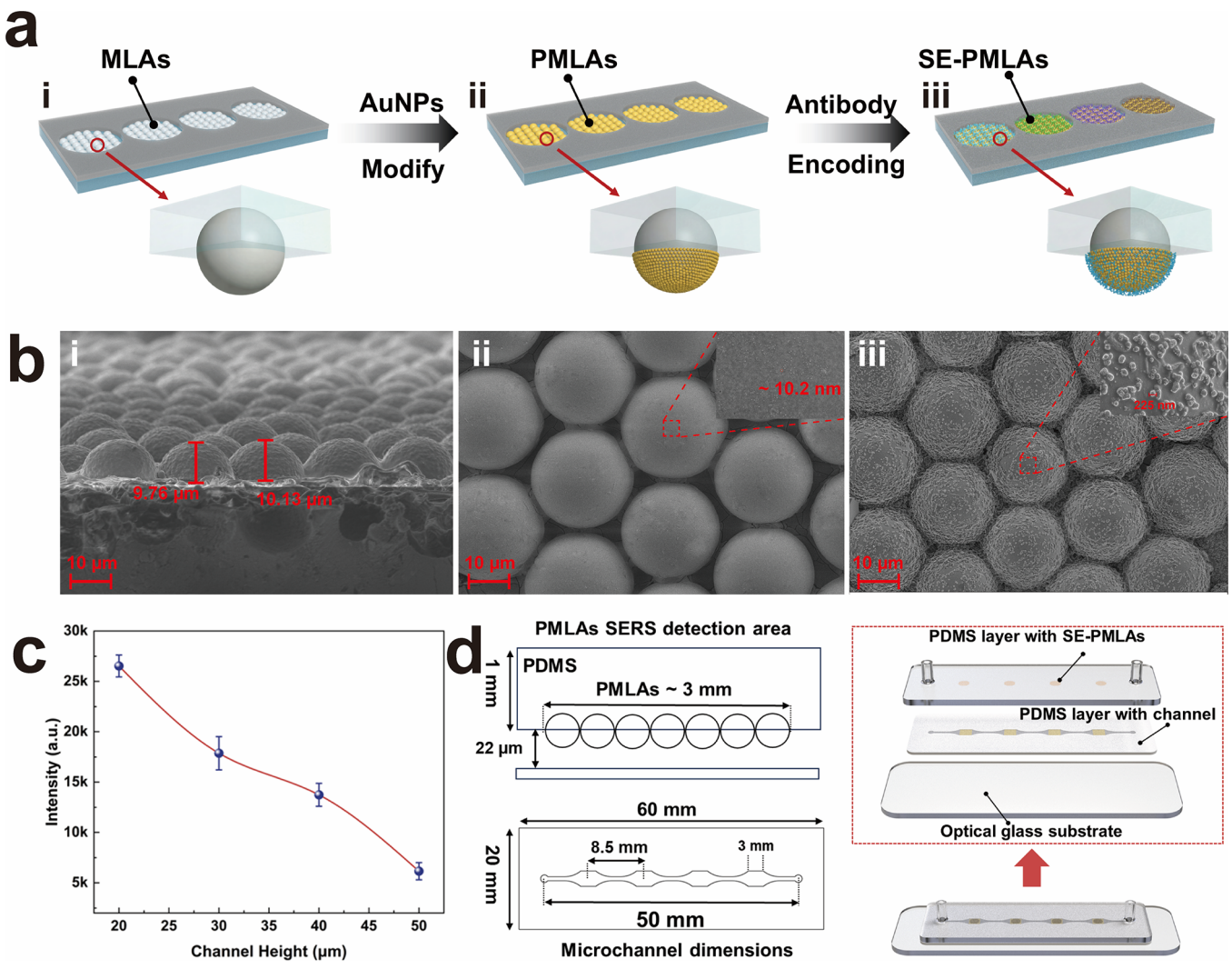

Figure 3. Fabrication and characterization of SE-PMLAs optofluidics SERS chip. (a) Three-step method for preparing spatially coded PMLAs. (b) Representative SEM characterization: (i) microsphere lens embedding depth in PDMS; (ii) monolayer coverage of 10 nm AuNPs on microsphere lens surfaces; (iii) uniform dispersion of Mag@Au nanotags on antibody-conjugated PMLAs after target analyte capture. (c) Effect of microchannel height on SERS signals. (d) Schematic diagram and dimensional drawing of SE-PMLAs optofluidics SERS chip.

Downloaded from pubs.acs.org/ascef/article-pdf/doi/10.1021/acssensors.6c03453/6901836/se-2026-03453z.pdf by UNIV OF JINAN user on 29 October 2026

https://doi.org/10.1021/acssensors.6c03453
ACS Sens. XXXX, XXX, XXX–XXX

and reduces the background. An excessively low height, however, increases the difficulty of chip bonding and the risk of blockage. Comparing channel heights of 20, 30, 40, and 50 μm showed that SERS signal intensity increases monotonically as the height decreases (Figure 3c), yet a height of 10 μm lowered the fabrication yield and was prone to bubble entrapment and clogging during continuous injection. We therefore selected 20 μm as the optimal channel height. The microfluidic channel layer and the PMLA functional layer were then integrated onto an optical glass substrate by a two-step oxygen plasma bonding process, forming the chip structure in Figure 3d and Figure S10. To rule out optical crosstalk between the spatially encoded sensing regions, a geometric-optics analysis of the collection geometry was performed. Owing to the directional antenna effect, the Raman emission from each region is collimated into a narrow cone of $\pm 11.5^{\circ}$ and collected by the Raman probe at a working distance of 2 mm above the PMLAs. The cone expands enough to overlap a neighboring region only after propagating ≈13.55 mm normal to the chip surface, far exceeding the ≈2 mm collection distance, so optical crosstalk between adjacent regions is geometrically excluded (Figure S11).

SE-PMLAs Optofluidics SERS Chip for Multiplexed Viruses Sensing Experiments

To validate the cross-interference resistance of the four independent PMLAs sensing units integrated in the chip, we systematically conducted cross-validation experiments on high concentrations of Flu A, Flu B, ADV, and MPXV. As shown in Figure 4a–d, only the corresponding PMLA region of the target virus exhibits a significant SERS signal. The signals from the other three mismatched PMLA regions remain at background levels. This result fully confirms that no non-specific cross-adsorption or optical signal crosstalk was observed between the units of SE-PMLA, ensuring the accuracy of the subsequent multi-channel detection. Then, a mixture containing predetermined concentrations of four viruses was co-incubated with four corresponding immuno-Mag@Au nanotags to verify the multiple detection performance of SE-PMLA. The enriched immune complexes were subsequently introduced into the chip at an optimized flow rate. When the sample flows through the PMLAs regions on the chip, which are functionalized with different specific antibodies, the target molecules are specifically captured in the corresponding PMLAs regions through antigen-antibody interactions. This enabled one-step, simultaneous, and quantitative multiplexeddetection of all four viruses.

The LODs of the chip for Flu A, Flu B, ADV, and MPXV were determined to be 0.45 pg/mL, 102.09 copies/mL, 97.48 copies/mL, and 1.5 pg/mL, respectively (Figure 4e–h). Each virus exhibited excellent linear responses across broad dynamic ranges (spanning 0.001 to 1000 ng/mL for Flu A, 117 to 1.67×10^5 copies/mL for Flu B, 250 to 1×10^5 copies/mL for ADV, and 0.0028 to 1120 ng/mL for MPXV) with corresponding R^2 values of 0.999, 0.981, 0.991, and 0.991 (Figure 4i–l). These results demonstrate the platform's ability to achieve both high sensitivity and a wide quantification range. To further evaluate the reliability and practicality of the chip, ten additional chips were fabricated using the same process

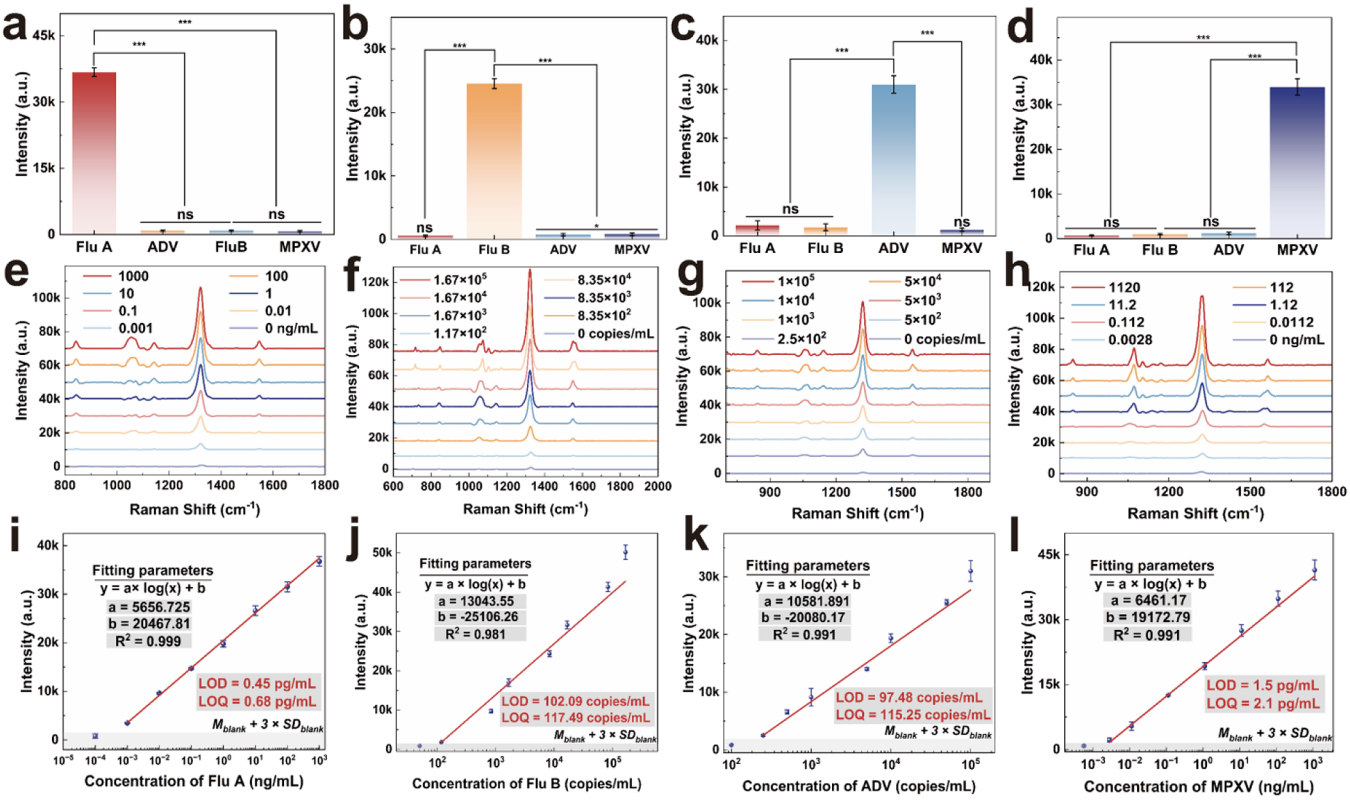

Figure 4. Performance validation of SE-PMLAs optofluidics SERS chip for multiplexed viruses detection. (a–d) Chip cross-validation experiments. Quantitative detection results for four target samples: (e–h) SERS spectra corresponding to different concentrations; (i–l) corresponding linear fitting results, detection ranges, and LODs.

Downloaded from pubs.acs.org/ascef/article-pdf/doi/10.1021/acssensors.6c03453/6901836/se-2026-03453z.pdf by UNIV OF JINAN user on 29 October 2026

https://doi.org/10.1021/acssensors.6c03453
ACS Sens. XXXX, XXX, XXX–XXX

following the quantitative detection. Under identical optimal conditions, independent repetitive tests were conducted for each type of virus at specific concentrations (Flu A: 0.1 ng/mL, Flu B: 8.35 × 10^3 copies/mL, ADV: 1 × 10^4 copies/mL, MPXV: 112 ng/mL). The results revealed that the RSD values for the ten independent measurements were 4.270% (Flu A), 4.471% (Flu B), 4.053% (ADV), and 3.944% (MPXV), with all RSD values consistently below 5% (Figure S12). This demonstrates the high stability and excellent repeatability of the platform in practical applications.

Sensing Performance of SE-PMLAs Optofluidics SERS Chip in Real Samples

To assess the practicality and stability of the chip in real diagnostic environments, we spiked healthy-volunteer throat swabs with the four viral antigens at the same concentration gradients as Figure 4e–h, incubated them with the immuno-Mag@Au nanotags, magnetically enriched the immune complexes, and injected them onto the chip (Figure 5a). The chip exhibited excellent linear responses for all four viruses in throat swabs (Figure 5b–i), with R^2 of 0.991 (Flu A), 0.988 (Flu B), 0.994 (ADV), and 0.987 (MPXV). Based on the spiked linear regression and the three-times-blank-standard-deviation method, the LODs in the complex matrix were 0.53 pg/mL, 128.85 copies/mL, 199.56 copies/mL, and 2.7 pg/mL, respectively, highly consistent with those in pure buffer owing to the integrated magnetic-enrichment and chip design, which purifies the sample and mitigates matrix background. Ten independent experiments further yielded inter-assay RSDs at three concentrations of 6.710%/4.462%/5.315%, 7.773%/5.616%/4.830%, 5.273%/6.125%/4.888%, and 7.405%/5.957%/7.215%, confirming robust reproducibility and reliability even in complex matrices (Figure 5j).

To validate the clinical diagnostic value of the chip, we collected pharyngeal swabs from 20 clinically diagnosed patients with suspected infections (Flu A: 6; Flu B: 8; ADV: 6) and 6 healthy controls, and tested all samples in parallel, double-blind with both the chip and qRT-PCR (CT ≤ 36 considered positive). The chip results showed high consistency (Figure 5k), and the receiver operating characteristic (ROC) analysis yielded an area under the curve (AUC) of 1 in this preliminary cohort (Figure 5l), indicating clear discrimination

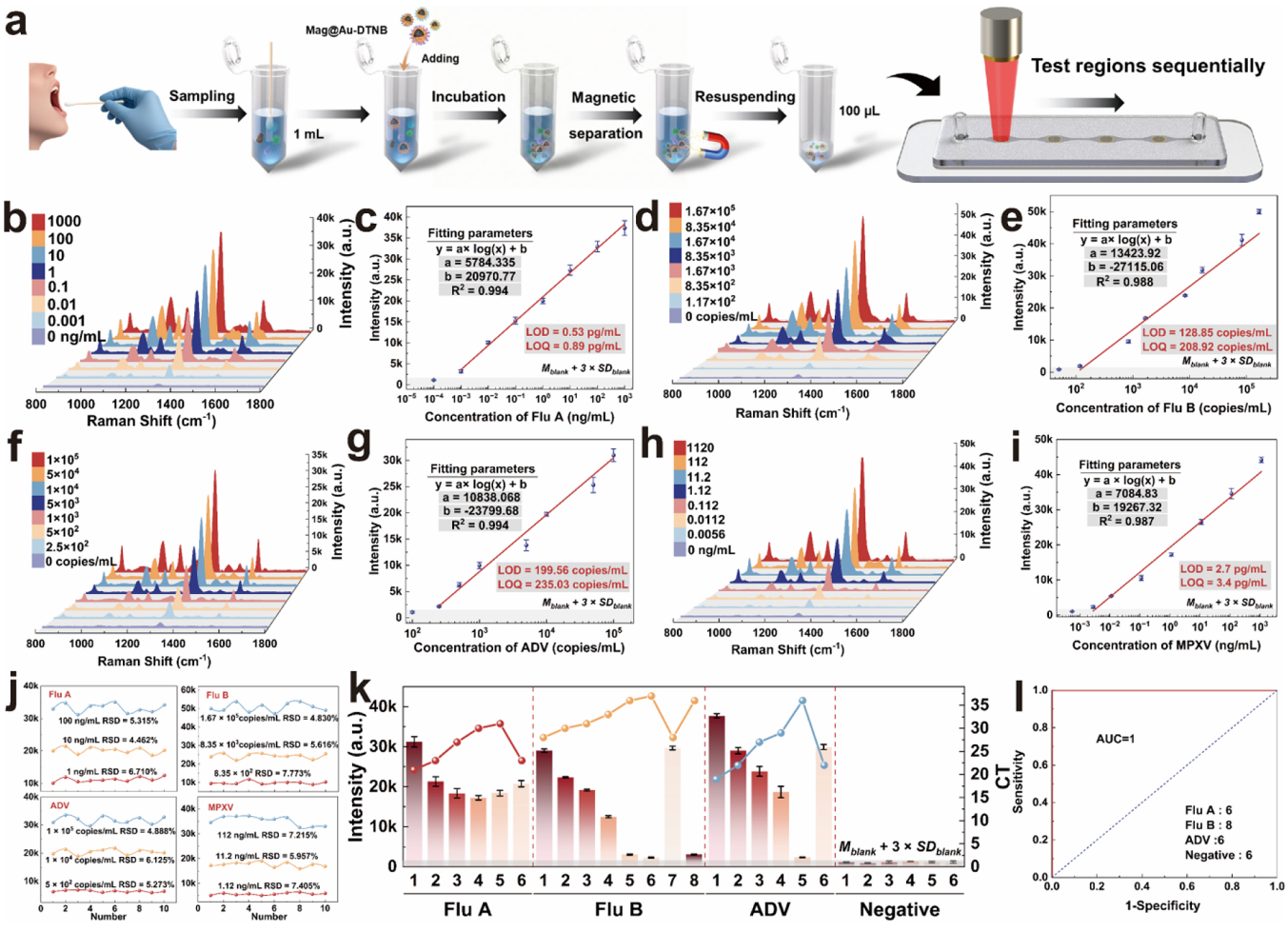

Figure 5. Practicality, robustness, and clinical validation of SE-PMLAs optofluidics SERS chip for multiplex viruses detection in real sample. (a) Schematic diagram of the processing workflow for throat swab samples. In the throat swab samples, SERS detection signals of four target viruses and their corresponding linear calibration curves: (b, c) Flu A, (d, e) FluB, (f, g) ADV, and (h, i) MPXV. (j) Ten independent experiments at three concentration levels for each virus, assessing the repeatability of chip detection. (k) Comparison of chip detection results with qRT-PCR results (with CT value ≤ 36 as the positive reference standard). (l) ROC curve based on clinical sample detection results, with an AUC of 1, indicating the chip's excellent disease discrimination diagnostic capability.

Downloaded from pubs.acs.org/ascef/article-pdf/doi/10.1021/acssensors.6c03453/6901836/se-2026-03453z.pdf by UNIV OF JINAN user on 29 October 2026

https://doi.org/10.1021/acssensors.6c03453
ACS Sens. XXXX, XXX, XXX–XXX

between the positive and negative groups in this limited sample set. These results demonstrate the feasibility of the chip for multiplex pathogen discrimination in clinical samples. Nevertheless, the sample size remains limited and the perfect AUC should be interpreted with caution, and a larger, multicenter cohort is warranted before clinical deployment. This work lays a solid technical foundation for next-generation multiplex, rapid, and quantitative pathogen detection.

SE-PMLAs Optofluidic SERS Chip Dynamics Monitoring Platform Based on the Initial Binding Rate Method

We engineered a dynamic monitoring platform based on the initial binding rate method (IBRM), leveraging the chip's sensitivity and multiplexing to overcome the time-consuming, kinetics-blind, and baseline-drift-prone limitations of endpoint assays. IBRM exploits the early stage of specific binding, when the solid-phase interface is unsaturated and the binding rate is constant. The captured target number and SERS intensity increase linearly with time, so the initial binding rate (the temporal derivative of signal) is directly proportional to concentration.[47]

For precise extraction, a Python pipeline expands a moving time window from the reaction onset and selects, as the optimal linear sampling interval, the longest window whose linear-regression R^2 remains ≥ 0.99 (Figures S13−S16), objectively removing subjective bias.

We applied this pipeline to Flu A, Flu B, ADV, and MPXV at the same concentration gradients as the standard assays, extracting initial binding rates from real-time curves (Figure 6a−h) and regressing them against concentration to build calibration curves (Figure 6i−l). The optimal linear sampling times (120, 80, 60, and 90 s) clustered within 60 to 120 s, far shorter than the > 10 min needed by endpoint methods to equilibrate, with R^2 of 0.982, 0.989, 0.981, and 0.976. This linear window is characterized by clear boundaries in concentration and in the environment. In concentration, two failure boundaries bracket the unsaturated-binding regime, the upper imposed by binding-site saturation and the lower by the noise floor. The dynamic range therefore equals the binding capacity to noise ratio, a concentration-dependent quantity that accounts for the signal roll-over at high concentrations and the noise-dominated fluctuation at low concentrations (the full derivation is given in the Supporting Information). In the environment, perturbation controls that varied only the temperature (5 to 50 °C) or the pH (4.5 to 8.5) showed that, within a ±10% quantification error (normalized rate 0.9 to 1.1), the four viruses shared a robust window of 17.5 to 37.8 °C and pH 5.8 to 7.8 (Figure S17). Outside this window, the kinetics slow or the antibody denatures (temperature), or interfacial interactions are disrupted (pH), lowering the normalized rate below 0.9. In addition, spike-and-recovery tests showed comparable recovery for both methods (standard and IBRM) but better precision for IBRM (mean CV 5.01% vs 6.61%, Table S1), because the early kinetic slope avoids long-term nonspecific adsorption and baseline drift.

Building on this robustness, continuous monitoring across a wide concentration gradient (Figure 6m−o) demonstrated that the IBRM linear ranges of 1×10^{-3} to 4×10^{5} ng/mL for Flu A and 1.17×10^{2} to 1.67×10^{6} copies/mL for Flu B markedly exceed those of the endpoint method, with average CVs of 4.70% and 3.45%, respectively (Table S2). Finally, a proof-of-concept using IL-6, one of the earliest and most dynamic inflammatory biomarkers, was realized by swapping the capture probe in one sensing region for an anti-human IL-6 antibody. This yielded concentration-dependent SERS signals (Figure 6p) and demonstrated that the platform extends to the rapid dynamic monitoring of protein biomarkers for real-time clinical diagnostics.

CONCLUSIONS

Conventional random SERS substrates partially mitigate signal fluctuations by statistical averaging in static detection, but in dynamic flow the stochastic hotspot distribution and the mismatch between micrometer-scale laser spots and fluidic channels amplify these limits. Anchoring AuNPs onto microsphere lenses created a deterministic plasmonic coupling system that spatially locks the PNJs, WGMs, and interparticle LSPR, converting stochastic signal generation into reproducible engineered hotspaces, while the directional-antenna effect enables efficient Raman collection. Beyond the hardware, an initial binding rate kinetic model quantifies targets by linear regression of signal intensity over time, using the early-stage unsaturated interface. It shortens detection to 1 to 2 min, mitigates baseline drift and binding-site saturation by relying on reaction rate rather than absolute intensity, and expands the linear dynamic range by two orders of magnitude. With spatial coding and microfluidics, the chip achieves simultaneous, single-injection, crosstalk-free multiplexed detection in complex clinical matrices.

In summary, we developed a spatially encoded photonic microlens array (SE-PMLAs) optofluidic SERS chip that addresses the trade-off between ultrahigh sensitivity and quantitative reproducibility, enabling a shift from static detection to real-time kinetic analysis (Table S3). Looking forward, two synergistic pathways will drive its evolution. Applications will expand from Raman-reporter-based detection toward label-free dynamic monitoring of viral replication and protein conformational changes for bedside critical care, home healthcare, and on-site biosafety screening. Hardware will be miniaturized into portable all-in-one devices or disposable cartridges. These dual drivers promise to transition the platform from a laboratory prototype into a transformative technology for public health and personalized medicine.

METHODS

Fabrication of SE-PMLAs Optofluidics SERS Chip

The fabrication of the SE-PMLAs optofluidics SERS chip involves template preparation, spatial encoding, and chip integration (Figures S18 and S19). First, PDMS is cast into a PMMA mold, pre-cured (100 °C, 5 min), masked with PET, embedded with microspheres via compression (5 min), and vacuum-sputtered with gold nanoparticles after full curing. Next, the surface is carboxylated via O_2 plasma, activated with an EDC/NHS buffer (15 min), incubated with distinct antibodies across four microregions (2.5 h, RT), and blocked with BSA (1.5 h, RT). Finally, an SU-8 mold is photolithographically fabricated (hard-baked 160 °C, 30 min) to cast PDMS microchannels (cured 80 °C, 2 h); after hole-punching, the PDMS channel layer, Au-silicon substrate, and PMLA assembly are bonded using O_2 plasma treatment (30 W, 30 s) and hermetically sealed via a 90 °C annealing step for 15 min.

Preparation of immuno-Mag@Au-DTNB Nanotags

The preparation of immuno-Mag@Au nanotags is shown in Figure S20. First, PEI-modified magnetic cores (Fe_3O_4@PEI) were synthesized by sonicating 2 mg of Fe_3O_4 microspheres with 2 mL of a 10 mg/mL aqueous PEI solution. Subsequently, this was sonicated with 35 mL of

Downloaded from pubs.acs.org/ascef/article-pdf/doi/10.1021/acssensors.6c03453/6901836/se-2026-03453z.pdf by UNIV OF JINAN user on 29 October 2026

https://doi.org/10.1021/acssensors.6c03453
ACS Sens. XXXX, XXX, XXX−XXX

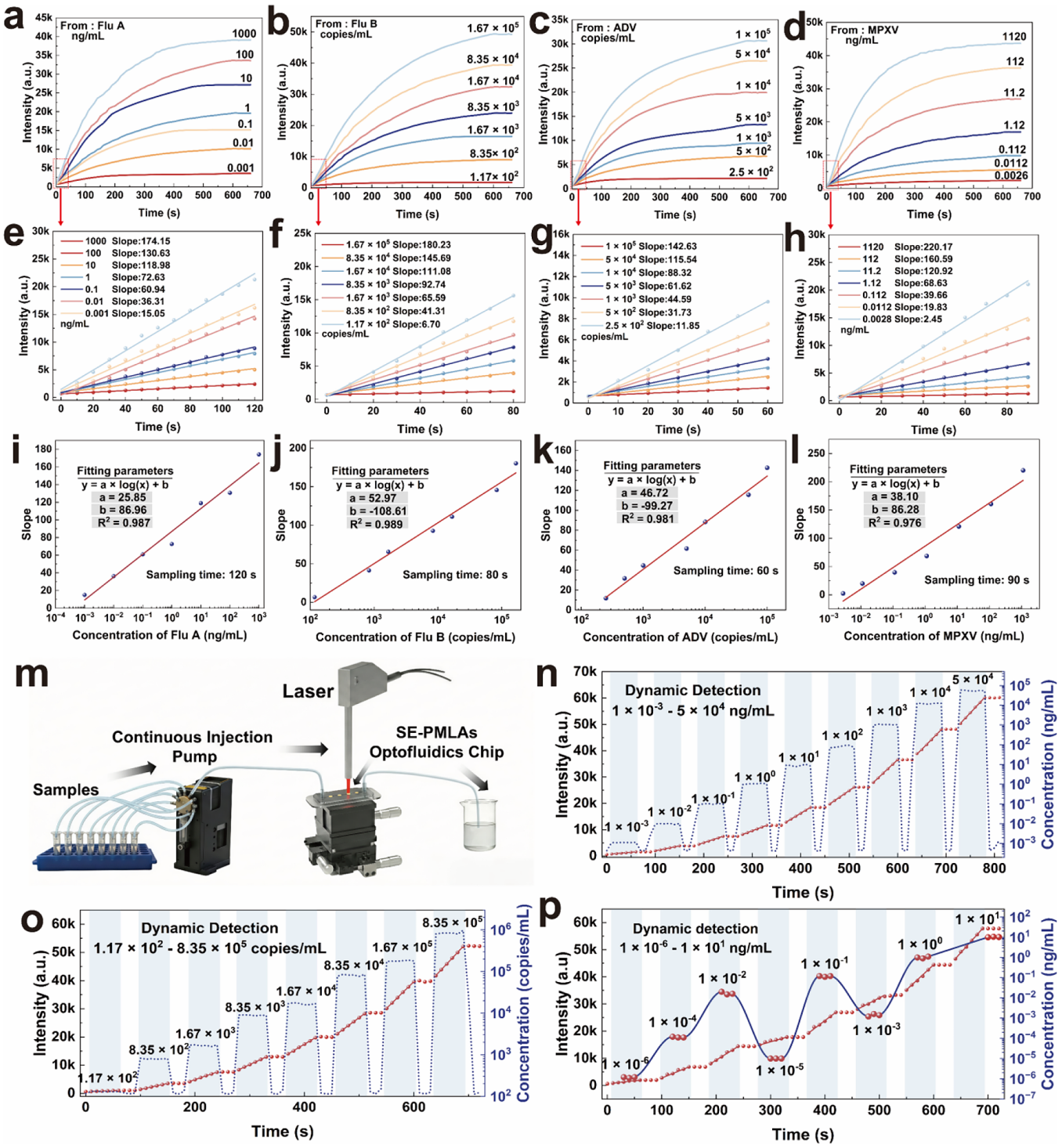

Figure 6. Performance evaluation of an initial binding rate method-based kinetic monitoring platform using SE-PMLAs optofluidic SERS chip. Real-time SERS signal intensity-time curves of Flu A (a), Flu B (b), ADV (c), and MPXV (d) at different concentration gradients. (e–h) Corresponding to the initial binding rate (slope) extraction results of each concentration curve in Figure 6 (a–d), for quantitative analysis. (i–l) Initial extraction rates of each target compound across different concentration gradients were linearly regressed against their corresponding known concentrations to establish quantitative calibration curves. (m) Continuous dynamic monitoring experimental platform. Using the Flu A (n) and Flu B (o) as a model for continuous monitoring, this demonstrates the advantage of the initial binding rate method over the endpoint method in extending the linear detection range. (p) IL-6 was selected as a model to demonstrate the feasibility of this chip and analytical method for clinical diagnosis.

Downloaded from pubs.acs.org/ascef/article-pdf/doi/10.1021/acssensors.6c03453/6901836/se-2026-03453z.pdf by UNIV OF JINAN user on 29 October 2026

https://doi.org/10.1021/acssensors.6c03453
ACS Sens. XXXX, XXX, XXX–XXX

a solution containing 13 nm gold nanoparticles synthesized by reducing chloroauric acid with sodium citrate to form Fe_3O_4-Au seeds; 2 mL of Mag-Au seed was added to 40 mL pure water dissolved 3 mg/mL PVP and 0.5 mg/mL $NH_2OH{\cdot}HCl$. Under ultrasonication, 150 μL of 1% HAuCl4 solution was added to grow the gold shell (Mag@Au). After magnetic separation, the product was ultrasonically encoded for 1 h in 40 mL of ethanol solution containing 30 μM DTNB. and the final product Mag@Au-DTNB was obtained after washing. Next, 1 mL of Mag@Au-DTNB tags was magnetically separated and resuspended in MEST buffer (0.1 M, pH 5.5, 0.01% Tween-20) followed by activation of surface carboxyl groups with a 5:1 mixture of EDC (10 0mM) and NHS (10 mM). After 15 min of vigorous ultrasonication, the activated SERS tags was transferred to 0.5 mL of PBST (pH 7.4, 0.05% Tween-20) containing 15 μg of detection antibody for 2 h. Unreacted carboxyl sites were blocked with 200 μL of 10% BSA (w/v) for 1.5 h. The synthesized immuno-Mag@Au nanotags was washed twice with PBST buffer and finally resuspended in 0.2 ml of PBST buffer containing 0.02% NaN3 for later use.

Parameter Optimization Experiment

To optimize detection, key parameters were systematically evaluated using signal-to-noise ratios. For magnetic enrichment, the optimal Mag@Au nanotag volume was 15 μL (Figure S21), with a 20-min viral incubation time ensuring efficient target capture (Figure S22). On the sensor interface, optimal PMLAs-modified antibody concentrations were determined as 20, 15, 20, and 20 μg/mL for Flu A, Flu B, ADV, and MPXV, respectively (Figure S23). Under the initial-rate method, a 10 μL/min injection flow rate provided the best balance of transport and reaction kinetics (Figure S24 and S25).Therefore, its detection conditions (such as antibody modification concentration) were derived from references.[48]

COMSOL Finite Element Simulation Analysis

The electromagnetic characteristics of PMLAs were investigated through finite element simulations using COMSOL Multiphysics. The model captured several representative light-matter interaction effects, such as PNJs, WGMs, directional antenna behavior, and LSPR coupling between neighboring Au nanoparticles. In the simulations, the microspheres were composed of barium titanate ($BaTiO_3$), whereas Mag@Au was modeled as a hybrid nanocomposite of Fe_3O_4 and Au. The multilayer environment consisted of PDMS and water as the upper and lower background media, respectively. The excitation wavelength was fixed at 785 nm. Perfectly matched layers were implemented at all model boundaries to suppress spurious reflections, and the outermost layerwas defined as an ideal conductor. The electromagnetic field was solved in the frequency domain with light propagation enabled throughout the space. A mixed meshing strategy (combining free triangular and mapped elements) was employed, maintaining mesh element sizes between λ/7 and λ/8 to ensure numericalaccuracy and convergence.

SERS Detection

Samples enriched by immuno-Mag@Au nanotags are pumped into the SE-PMLAs chip and captured by four antibody-encoded regions. Raman signals (785 nm, 5 mW, 1 s × 3 accumulations) are collected, processed in Python 3.11, and quantified via Origin 2025. For dynamic monitoring, an automated pump sequentially injects gradient samples while real-time SERS signals are continuously recorded (3 s sampling, 10 s interval) to track molecular binding.

■ ASSOCIATED CONTENT

Supporting Information

The Supporting Information is available free of charge at https://pubs.acs.org/doi/10.1021/acssensors.6c03453.

The materials and instruments; The theoretical derivations include the calculation of AEF and the Langmuir-kinetics derivation of the IBRM failure boundaries; The figures (S1−S25) include the optical simulations of AuNP size effects on the PNJ/WGM/directional antenna effect, chip fabrication and characterization, immuno-Mag@Au preparation, sampling-window and temperature/pH robustness, condition optimization, and flow simulation; The tables (S1−S3) include the spiked-recovery comparison between the endpoint and initial-rate methods, the continuous dynamic quantification results, and the performance comparison with other biosensors (DOCX)

■ AUTHOR INFORMATION

Corresponding Authors

Yan-Qing Lu − *Key Laboratory of Intelligent Optical Sensing and Integration of the Ministry of Education, College of Engineering and Applied Sciences, Nanjing University, Nanjing 210093, China;* orcid.org/0000-0001-6151-8557; Email: yqlu@nju.edu.cn

Rui Xiao − *State Key Laboratory of Pathogen and Biosecurity, Beijing Institute of Microbiology and Epidemiology, Beijing 100071, China;* orcid.org/0000-0002-6313-4757; Email: ruixiao203@163.com

Guanghui Wang − *Key Laboratory of Intelligent Optical Sensing and Integration of the Ministry of Education, College of Engineering and Applied Sciences, Nanjing University, Nanjing 210093, China; Department of Clinical Laboratory, Nanjing Drum Tower Hospital, Affiliated Hospital of Medical School, Nanjing University, Nanjing 210008, China;* orcid.org/0000-0002-6832-7937; Email: wangguanghui@nju.edu.cn

Authors

Zhenyong Dong − *Key Laboratory of Intelligent Optical Sensing and Integration of the Ministry of Education, College of Engineering and Applied Sciences, Nanjing University, Nanjing 210093, China; Institute for Advanced Interdisciplinary Research, School of Chemistry and Chemical Engineering, University of Jinan, Jinan 250022, China;* orcid.org/0000-0002-4192-5638

Xiaoxian Liu − *State Key Laboratory of Pathogen and Biosecurity, Beijing Institute of Microbiology and Epidemiology, Beijing 100071, China; College of Veterinary Medicine, Anhui Agricultural University, Hefei 230036, China*

Tao Wu − *NHC Key Laboratory of Enteric Pathogenic Microbiology, Jiangsu Provincial Center for Disease Control and Prevention, Nanjing 210009, China*

Feixiang Zheng − *Key Laboratory of Intelligent Optical Sensing and Integration of the Ministry of Education, College of Engineering and Applied Sciences, Nanjing University, Nanjing 210093, China*

Yukai Liu − *Key Laboratory of Intelligent Optical Sensing and Integration of the Ministry of Education, College of Engineering and Applied Sciences, Nanjing University, Nanjing 210093, China*

Xiao Ren − *Key Laboratory of Intelligent Optical Sensing and Integration of the Ministry of Education, College of Engineering and Applied Sciences, Nanjing University, Nanjing 210093, China*

Feng Xu − *School of Information Engineering, Yancheng Institute of Technology, Yancheng 224051, China*

Downloaded from pubs.acs.org/ascef/article-pdf/doi/10.1021/acssensors.6c03453/6901836/se-2026-03453z.pdf by UNIV OF JINAN user on 29 October 2026

https://doi.org/10.1021/acssensors.6c03453
ACS Sens. XXXX, XXX, XXX−XXX

Lunbiao Cui − *NHC Key Laboratory of Enteric Pathogenic Microbiology, Jiangsu Provincial Center for Disease Control and Prevention, Nanjing 210009, China*

Complete contact information is available at: https://pubs.acs.org/doi/10.1021/acssensors.6c03453

Author Contributions

‡Z.D. and X.L. contributed equally to this work. Z.D.: Conceptualization, methodology, data curation, validation, writing−original draft, and writing−review and editing. X.L.: Conceptualization, methodology, writing−review and editing, and funding acquisition. T.W.: Methodology. F.Z.: Methodology. Y.L.: Resources. X.R.: Resources. F.X.: Resources. L.C.: Resources. Y.-Q.L.: Conceptualization, methodology, and writing−review and editing. R.X.: Conceptualization, methodology, and writing−review and editing. G.W.: Conceptualization, methodology, writing−review and editing, and funding acquisition.

Notes

The authors declare no competing financial interest.

■ ACKNOWLEDGMENTS

This work was supported by the National Natural Science Foundation of China (62375121), The Frontier Technologies R&D Program of Jiangsu (BF2025633, BF2025020). China Postdoctoral Science Foundation (2025M783033).

■ REFERENCES

(1) Sempionatto, J. R.; Lasalde-Ramirez, J. A.; Mahato, K.; Wang, J.; Gao, W. Wearable chemical sensors for biomarker discovery in the omics era. *Nat. Rev. Chem.* **2022**, *6* (12), 899−915.

(2) Cho, S.; Shajari, S.; Xiong, Y.; Madsen, K.; Lv, Z.; Cho, S.; Park, J.; Li, M.; Li, S.; Feng, L.; et al. Wearable lateral flow assays for cortisol monitoring with time-dynamic sweat sampling and sensing by electrochromic timers. *Nat. Sens.* **2026**, *1* (1), 85−98.

(3) Herbst, R. S.; John, T.; Grohe, C.; Goldman, J. W.; Kato, T.; Laktionov, K.; Bonanno, L.; Tiseo, M.; Majem, M.; Domine, M.; et al. Molecular residual disease analysis of adjuvant osimertinib in resected EGFR-mutated stage IB-IIIA non-small-cell lung cancer. *Nat. Med.* **2025**, *31* (6), 1958−1968.

(4) Donnelly, J. M.; Neff, R. A.; Sedlack, A. J. H.; Juska, V. B.; Ayala-Cardona, L. F.; Bass, J.; McNally, E. M.; Shah, S. J.; Alshurafa, N.; Kimchi, E. Y.; et al. From reactive to proactive: Continuous protein monitoring for preventive health care. *Science* **2025**, *389* (6767), No. eady6497.

(5) Liu, R.; Li, J.; Salena, B. J.; Li, Y. Aptamer and DNAzyme Based Colorimetric Biosensors for Pathogen Detection. *Angew. Chem., Int. Ed. Engl.* **2025**, *64* (4), No. e202418725.

(6) Cao, Y.; Lau, P. N.; Chin, A. W. H.; He, Z.; Au Yeung, C. C. K.; Zeng, K.; Lin, H.; Poon, L. L. M.; Shum, H. C. A Phase Separation-Assisted Pre-Enrichment Method for Ultrasensitive Respiratory Virus Detection. *Adv. Sci.* **2025**, *12* (36), No. e06578.

(7) Chang, H.; Hur, W.; Kang, H.; Jun, B. H. In vivo surface-enhanced Raman scattering techniques: nanoprobes, instrumentation, and applications. *Light: Sci. Appl.* **2025**, *14* (1), 79.

(8) Song, L.; Jiang, S.; Huang, L.; Chen, L.; Liu, X.; Gong, E.; Yuan, N.; Jian, S.; Huang, Y. Analyte-Targeted Plasmonic Hotspots on Superlattice Mirror Enable Ultra-Broad-Range SERS Sensing of Acetylcholinesterase. *Angew. Chem., Int. Ed. Engl.* **2025**, *13* (5), No. e21361.

(9) Bi, X.; Czajkowsky, D. M.; Shao, Z.; Ye, J. Digital colloid-enhanced Raman spectroscopy by single-molecule counting. *Nature* **2024**, *628* (8009), 771−775.

(10) Son, W. K.; Choi, Y. S.; Han, Y. W.; Shin, D. W.; Min, K.; Shin, J.; Lee, M. J.; Son, H.; Jeong, D. H.; Kwak, S. Y. In vivo surface-enhanced Raman scattering nanosensor for the real-time monitoring of multiple stress signalling molecules in plants. *Nat. Nanotechnol.* **2023**, *18* (2), 205−216.

(11) Jin, Z.; Chen, S.; Dong, X.; Zhao, Z.; Zeng, H.; Zhang, P.; Yin, H.; Zhou, S.; Li, C.; He, C.; et al. Label-free navigation system for grading prostate tumour malignancy in situ via tissue pH and prostate-specific antigen activity. *Nat. Biomed. Eng.* **2025**, 1871.

(12) Shin, H.; Choi, B. H.; Shim, O.; Kim, J.; Park, Y.; Cho, S. K.; Kim, H. K.; Choi, Y. Single test-based diagnosis of multiple cancer types using Exosome-SERS-AI for early stage cancers. *Nat. Commun.* **2023**, *14* (1), 1644.

(13) Chen, T.; Xin, J.; Chang, S. J.; Chen, C. J.; Liu, J. T. Surface Plasmon Resonance (SPR) Combined Technology: A Powerful Tool for Investigating Interface Phenomena. *Adv. Mater. Interfaces* **2023**, *10* (8), No. 2202202.

(14) Jodaylami, M. H.; Masson, J.-F.; Badia, A. Surface plasmon resonance sensing. *Nat. Rev. Methods Primers* **2025**, *5* (1), 47.

(15) Chang, S.; Li, Z.; Liu, L.; Wang, C.; Wang, J.; Nie, A.; Wen, F.; Mu, C.; Zhai, K.; Xiang, J.; et al. Atomic-Level Defect Engineering in GeP Nanoflake Biosensors for Gastric Cancer Diagnosis. *ACS Nano* **2024**, *18* (40), 27547−27556.

(16) Li, R.; Zhou, Y.; Chen, Y.; Zhou, L.; Yang, Y.; Xiao, J.; Liu, G. L.; Wang, J.; Huang, L.; Li, Y. High-Electron-Mobility MXene-Enhanced Metasurface Biosensors Integrated with Microfluidics for Real-Time Multifunctional Monitoring. *ACS Nano* **2025**, *19* (12), 12007−12020.

(17) Li, W.; Chen, M.; Chen, Y.; Yang, Y.; Ruan, J.; Chang, J.; Li, J.; Liu, G. L.; Hu, W. Metasurface plasmon resonance platform for high-throughput, label-free, real-time, long-term monitoring of in vitro cancer therapy assessment. *Biosens. Bioelectron.* **2026**, *292*, No. 118052.

(18) Fan, H.; Li, R.; Chen, Y.; Da, Q.; Xiong, C.; Zhang, Y.; Qin, Z.; Liu, G. L.; Huang, L. Sample-to-answer point-of-care testing platform for quantitative detection of small molecules in blood using a smartphone-and microfluidic-based nanoplasmonic biosensor. *Chem. Eng. J.* **2024**, *501*, No. 157495.

(19) Zhang, S.; Han, B.; Zhang, Y. n.; Liu, Y.; Zheng, W.; Zhao, Y. Multichannel Fiber Optic SPR Sensors: Realization Methods, Application Status, and Future Prospects. *Laser Photonics Rev.* **2022**, *16* (8), No. 2200009.

(20) Gao, D.; Liu, J.; Liu, X.; He, K.; Ma, Z.; Liu, H.; Wang, J.; Zhang, Q.; Huang, Z.; Luo, M.; et al. Emerging frontiers in SERS-integrated optical waveguides: advancing portable and ultra-sensitive detection for trace liquid analysis. *Light: Sci. Appl.* **2025**, *14* (1), 389.

(21) Jiang, S.; Xiao, Y.; Li, Q.; Jiang, L.; Wu, J.; Li, Y. SERS technology in virus Detection: Advances, challenges, and future perspectives. *Biosens. Bioelectron.* **2025**, *290*, No. 117902.

(22) Cialla-May, D.; Bonifacio, A.; Markin, A.; Markina, N.; Fornasaro, S.; Dwivedi, A.; Dib, T.; Farnesi, E.; Liu, C.; Ghosh, A.; et al. Recent advances of surface enhanced Raman spectroscopy (SERS) in optical biosensing. *TrAC, Trends Anal. Chem.* **2024**, *181*, No. 117990.

(23) Zou, Y.; Jin, H.; Ma, Q.; Zheng, Z.; Weng, S.; Kolataj, K.; Acuna, G.; Bald, I.; Garoli, D. Advances and applications of dynamic surface-enhanced Raman spectroscopy (SERS) for single molecule studies. *Nanoscale* **2025**, *17* (7), 3656−3670.

(24) Li, G.; Zhao, X.; Tang, X.; Yao, L.; Li, W.; Wang, J.; Liu, X.; Han, B.; Fan, X.; Qiu, T.; et al. Wearable Hydrogel SERS Chip Utilizing Plasmonic Trimers for Uric Acid Analysis in Sweat. *Nano Lett.* **2024**, *24* (42), 13447−13454.

(25) Cong, L.; Wang, J.; Li, X.; Tian, Y.; Xu, S.; Liang, C.; Xu, W.; Wang, W.; Xu, S. Microfluidic Droplet-SERS Platform for Single-Cell Cytokine Analysis via a Cell Surface Bioconjugation Strategy. *Anal. Chem.* **2022**, *94* (29), 10375−10383.

(26) Diao, X.; Li, X.; Hou, S.; Li, H.; Qi, G.; Jin, Y. Machine Learning-Based Label-Free SERS Profiling of Exosomes for Accurate Fuzzy

Downloaded from pubs.acs.org/ascef/article-pdf/doi/10.1021/acssensors.6c03453/6901836/se-2026-03453z.pdf by UNIV OF JINAN user on 29 October 2026

Diagnosis of Cancer and Dynamic Monitoring of Drug Therapeutic Processes. *Anal. Chem.* **2023**, *95* (19), 7552−7559.
(27) Wang, L. C.; Kuo, Y. C.; Kuo, Y. T.; Chang, K. L.; Chen, Y. C.; Wang, W. J.; Hung, M. Y.; Hsu, F. Y.; Aich, P.; Lin, Y. W.; et al. Utilizing Electron-Sink-Enhanced Nanoshells for Amplified Nanoplasmonic SERS-Based In Situ Detection of Cancer Cells, Linking Signal Enhancement with Cellular Damage. *Adv. Mater.* **2025**, *37* (20), No. e2417950.
(28) Dong, P.; Xiong, S.; Gong, Y.; Wang, C.; Li, X.; Wu, X. SERS-based pump-free microfluidic chip sensor for immunoassays of the myocardial injury marker CK-MB. *Sens. Actuators, B* **2026**, *451*, No. 139397.
(29) Chen, X.; Tang, J.; Zhao, Y.; Wang, R.; Sang, S.; Yu, F.; Xing, Y. Sensitive phenotyping of serum extracellular vesicles on a SERS-microfluidic platform for early-stage clinical diagnosis of ovarian carcinoma. *Biosens. Bioelectron.* **2025**, *267*, No. 116724.
(30) Chen, M.; Liu, G.; Wang, L.; Zhang, A.; Yang, Z.; Li, X.; Zhang, Z.; Gu, S.; Cui, D.; Haick, H.; et al. Neural Network-Enhanced Electrochemical/SERS Dual-Mode Microfluidic Platform for Accurate Detection of Interleukin-6 in Diabetic Wound Exudates. *Anal. Chem.* **2025**, *97* (8), 4397−4406.
(31) Zhang, D.; Peng, K.; Xu, H.; Chen, Y.; Wang, J. Proteomics-Empowered Microfluidic-SERS Immunoassay for Identifying and Detecting Biomarkers of Micropapillary Lung Adenocarcinoma. *Adv. Sci.* **2025**, *12* (25), No. e2501336.
(32) Zhan, C.; Yang, D.; Gao, R.; Wang, Y.; Xu, M.; Lu, Y.; Jia, H.; Feng, Y.; Yu, L. Molecular Recognition and Topological Matching of CTCs on the Novel Bioinspired Hierarchically Functional Interface with SERS-Microfluidic Sensors. *ACS Sens.* **2025**, *10* (11), 8531−8541.
(33) Lyu, N.; Hassanzadeh-Barforoushi, A.; Zhang, W.; Ngo, C. H. L.; Hnit, S. S. T.; Inglis, D. W.; Wang, Y. On-Chip Profiling of Bacterially Infected Host Cell-Derived Small Extracellular Vesicles by Surface-Enhanced Raman Scattering. *ACS Nano* **2026**, *20* (1), 1481−1491.
(34) Lin, L. L.; Alvarez-Puebla, R.; Liz-Marzan, L. M.; Trau, M.; Wang, J.; Fabris, L.; Wang, X.; Liu, G.; Xu, S.; Han, X. X.; et al. Surface-Enhanced Raman Spectroscopy for Biomedical Applications: Recent Advances and Future Challenges. *ACS Appl. Mater. Interfaces* **2025**, *17* (11), 16287−16379.
(35) Zhang, J.; Xu, L.; Hu, Y.; Sun, L.; Xie, Y.; Miao, X.; Liu, A.; Hou, Z.; Gou, Y.; Wu, A.; et al. Integrating Inertial Microfluidics with SERS Bioprobe for Efficient Enrichment and Accurate Identification of Tumor Cells in Gastric Fluid and Ascites. *Anal. Chem.* **2025**, *97* (26), 13901−13911.
(36) Sun, N.; Gan, Y.; Wu, Y.; Wang, X.; Shen, S.; Zhu, Y.; Zhang, J. Single-beam optical trap-based surface-enhanced Raman scattering optofluidic molecular fingerprint spectroscopy detection system. *Opto-Electron. Adv.* **2025**, *8* (2), No. 240182.
(37) Geints, Y. E.; Zemlyanov, A. A.; Minin, O. V.; Minin, I. V. Systematic study and comparison of photonic nanojets produced by dielectric microparticles in 2D- and 3D-spatial configurations. *J. Opt.* **2018**, *20* (6), No. 065606.
(38) Yang, H.; Trouillon, R.; Huszka, G.; Gijs, M. A. Super-Resolution Imaging of a Dielectric Microsphere Is Governed by the Waist of Its Photonic Nanojet. *Nano Lett.* **2016**, *16* (8), 4862−4870.
(39) Zhang, P.; Yan, B.; Gu, G.; Yu, Z.; Chen, X.; Wang, Z.; Yang, H. Localized photonic nanojet based sensing platform for highly efficient signal amplification and quantitative biosensing. *Sens. Actuators, B* **2022**, *357*, No. 131401.
(40) Gašparić, V.; Taccheo, S.; Gebavi, H.; Ristić, D.; Ivanda, M. Photonic nanojet mediated Raman enhancement: Vertical Raman mapping and simple ray matrix analysis. *J. Raman Spectrosc.* **2019**, *51* (1), 165−175.
(41) Guo, J.; Wu, Y.; Gong, Z.; Chen, X.; Cao, F.; Kala, S.; Qiu, Z.; Zhao, X.; Chen, J. J.; He, D.; et al. Photonic Nanojet-Mediated Optogenetics. *Adv. Sci.* **2022**, *9* (12), 2104140.
(42) Ruzankina, I.; Mukhin, N.; Mermoul, A.; Parfenov, V.; Fron, E.; Ferrini, G. Surface optical sensitivity enhanced by a single dielectric microsphere. *Opt. Express* **2022**, *30* (24), 43021−43036.
(43) Yan, Y.; Xing, C.; Jia, Y.; Zeng, Y.; Zhao, Y.; Jiang, Y. Self-assembled dielectric microsphere array enhanced Raman scattering for large-area and ultra-long working distance confocal detection. *Opt. Express* **2015**, *23* (20), 25854−25865.
(44) Dong, Z.; Liu, X.; Zhou, S.; Zhu, Y.; Chen, J.; Liu, Y.; Ren, X.; Lu, Y. Q.; Xiao, R.; Wang, G. Microsphere lens array embedded microfluidic chip for SERS detection with simultaneous enhancement of sensitivity and stability. *Biosens. Bioelectron.* **2024**, *261*, No. 116505.
(45) Dong, Z.; Zheng, F.; Wang, H.; Liu, Y.; Ren, X.; Lin, F.; Zhou, S.; Chen, L.; Lu, Y. Q.; Wang, G. Plasmonic microsphere lens arrays-integrated microfluidic SERS chip for mixed pesticides identification with machine learning. *J. Hazard. Mater.* **2025**, *501*, No. 140994.
(46) Bao, H.; E. X. T.; Zhou, J.; Zhao, X.; Leong, S. Y.; Chek, C. H.; Leon, G. K.; Chen, J. R. T.; Nguyen, L. B. T.; Li, L.; Hou, H. W.; Zhang, H.; Phang, I. Y.; Ling, X. Y. From hotspots to hotspaces: Cascaded photonic-plasmonic coupling for SERS-based deep profiling of whole small extracellular vesicles. *Sci. Adv.* **2026**, *12*, No. eaec2026.
(47) Yue, X.; Yan, S.; Gao, T.; Pu, S.; Tang, H.; Pei, X.; Tian, Z.; Wang, X.; Ren, B.; Liu, G. SERS Performance Factor: A Convenient Parameter for the Enhancement Evaluation of SERS Substrates. *Anal. Chem.* **2024**, *96* (44), 17517−17525.
(48) Zhou, X.; Li, P.; Wu, X.; Lin, X.; Zhao, L.; Huang, H.; Wu, J.; Cai, H.; Xu, M.; Zhou, H.; et al. Multifunctional biosensor constructed by Ag-coating magnetic-assisted unique urchin core porous shell structure for dual SERS enhancement, enrichment, and quantitative detection of multi-components inflammatory markers. *Biosens. Bioelectron.* **2022**, *210*, No. 114257.

Downloaded from pubs.acs.org/ascef/article-pdf/doi/10.1021/acssensors.6c03453/6901836/se-2026-03453z.pdf by UNIV OF JINAN user on 29 October 2026

https://doi.org/10.1021/acssensors.6c03453
ACS Sens. XXXX, XXX, XXX−XXX